



# Spallation-altered Accreted Compositions for X-Ray Bursts: Impact on Ignition Conditions and Burst Ashes

J. S. Randhawa<sup>1,2</sup> , Z. Meisel<sup>3</sup> , S. A. Giuliani<sup>2</sup>, H. Schatz<sup>2,4,5</sup>, B. S. Meyer<sup>6</sup>, K. Ebinger<sup>7</sup> , A. A. Hood<sup>8</sup>, and R. Kanungo<sup>1</sup>

<sup>1</sup>Department of Astronomy and Physics, Saint Mary's University, 923 Robie Street, Halifax, NS B3H 3C3, Canada; [randhawa@nscl.msu.edu](mailto:randhawa@nscl.msu.edu)

<sup>2</sup>National Superconducting Cyclotron Laboratory, Michigan State University, East Lansing, MI 48824, USA

<sup>3</sup>Institute of Nuclear and Particle Physics, Department of Physics & Astronomy, Ohio University, Athens, OH 45701, USA

<sup>4</sup>Department of Physics and Astronomy, Michigan State University, East Lansing, MI 48824, USA

<sup>5</sup>JINA Center for the Evolution of the Elements, Michigan State University, East Lansing, MI 48824, USA

<sup>6</sup>Department of Physics and Astronomy, Clemson University, Clemson, SC 29634-0978, USA

<sup>7</sup>GSI Helmholtzzentrum für Schwerionenforschung, D-64291 Darmstadt, Germany

<sup>8</sup>Department of Physics and Astronomy, Louisiana State University, Baton Rouge, LA 70803, USA

Received 2019 August 24; revised 2019 October 16; accepted 2019 October 17; published 2019 December 13

## Abstract

Model predictions of X-ray burst ashes and light curves depend on the composition of the material accreted from the companion star, in particular the abundance of CNO elements. It has previously been pointed out that spallation in the atmosphere of the accreting neutron star can destroy heavy elements efficiently. In this work we study this spallation using a realistic reaction network that follows the complete spallation cascade and takes into account not only destruction, but also production of elements by the spallation of heavier species. We find an increased survival probability of heavier elements compared to previous studies, resulting in significantly higher CNO abundances. We provide resulting compositions as a function of accretion rate, and explore their impact on 1D multi-zone X-ray burst models. We find significant changes in the composition of the burst ashes, which will affect the thermal and compositional structure of accreted neutron star crusts.

*Unified Astronomy Thesaurus concepts:* X-ray bursts (1814); X-ray bursters (1813)

## 1. Introduction

Thermonuclear explosions on the surface of accreting neutron stars in low-mass X-ray binaries give rise to Type I X-ray bursts (Lewin et al. 1993; Schatz & Rehm 2006; Jose 2016; Meisel et al. 2018). These are among the most frequent thermonuclear explosions in nature with recurrence times ranging from hours to days (Strohmayer & Bildsten 2006). X-ray bursts are powered by nuclear reaction sequences that include the triple- $\alpha$ -process, the  $\alpha$   $p$ -process, and the rapid proton capture process ( $rp$ -process; Wallace & Woosley 1981; Woosley et al. 2004; Schatz & Rehm 2006; Fisker et al. 2008; José et al. 2010; Cyburt et al. 2016). X-ray burst observations can serve as important probes of neutron stars (Cumming et al. 2006; Zamfir et al. 2012; Özel & Freire 2016). However, to interpret observations in terms of neutron star properties requires reliable burst models. These models depend on a range of input parameters, including the composition of the accreted material (Woosley et al. 2004; Heger et al. 2007; José et al. 2010). This composition strongly affects ignition conditions and the nuclear evolution during the burst (Wallace & Woosley 1981; Cumming & Bildsten 2000; Schatz et al. 2001; Woosley et al. 2004; José et al. 2010). Typical choices of accreted composition are based on the presumed composition of the companion star and range from solar-metallicity to metal-deficient ( $Z \sim 10^{-3}$ ; Cumming & Bildsten 2000; Schatz et al. 2001; Heger et al. 2007). It has been pointed out previously that proton-induced spallation of the accreted material in the neutron star atmosphere may change the accreted composition before it settles into the deeper layers of the neutron star (Bildsten et al. 1992). Due to Coulomb collisions with atmospheric electrons, heavier elements thermalize at shallower depths compared to hydrogen and helium. At these shallower depths incoming protons still have high

enough energies to destroy the heavier elements through nuclear spallation reactions. In Bildsten et al. (1992) it was explicitly mentioned that spallation of the thermalized ions by protons leads to nuclear fragments, which can further undergo fragmentation, hence resulting in a cascading destruction process. Due to lack of knowledge of the relevant spallation cross sections at that time, only the isolated destruction of CNO elements was discussed. Here we study for the first time the full cascading production and destruction processes using a full nuclear reaction network.

In Section 2 we introduce our model, in Section 3 we present our results of the final composition as a function of accretion rate, and in Section 4 we discuss the impact on a 1D multi-zone hydrodynamic X-ray burst model.

## 2. Method

The kinetic energy of free-falling material onto a  $1.4 M_{\odot}$  neutron star of 10 km radius is  $\sim 200 \text{ MeV u}^{-1}$ . Due to Coulomb collisions with atmospheric electrons, heavier elements thermalize at shallower depths compared to hydrogen and helium. At these shallower stopping depths, incoming protons still have high energies, exposing the heavy nuclei to a flux of energetic protons. The time for heavy elements to diffuse from their stopping depths to the proton stopping depth defines the duration of exposure to high-energy protons, the exposure time  $t_{\text{exposure}}$ .

We follow Bildsten et al. (1992) to obtain an estimate of  $t_{\text{exposure}}$ , which they referred to as  $t_{\text{res}}$ , or residence time. The loading time needed to replenish nuclei in the zone where heavier elements are exposed to proton irradiation depends on the range difference of protons and heavy nuclei and can be

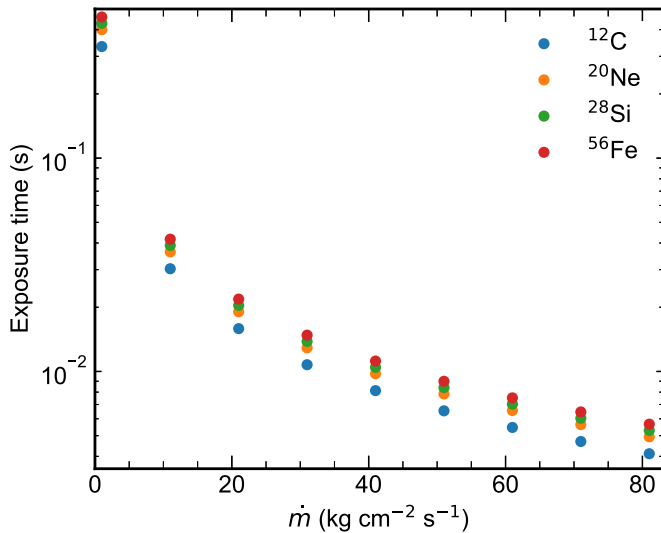


**Figure 1.** Exposure time for different elements as a function of mass accretion rate per unit area.  $10 \text{ kg cm}^{-2} \text{ s}^{-1}$  corresponds to  $2.5 \times 10^{-9}$  solar masses per year for a neutron star with 11.2 km of radius.

approximated (Equation (1.5) of Bildsten et al. 1992) as

$$t_{\text{load}} = \left(1 - \frac{A}{Z^2}\right) \frac{y_s(p)}{j_p}, \quad (1)$$

where  $j_p$  is the proton beam current,  $A$  and  $Z$  are mass and atomic numbers of a given element, respectively, and  $y_s(p)$  is the electron column density needed to stop protons. The average time a nucleus spends in this region is determined by diffusion and differs from  $t_{\text{load}}$  by factor  $R$ , i.e.,  $t_{\text{exposure}} = R \times t_{\text{load}}$ . Therefore,

$$t_{\text{exposure}} = \frac{R}{j_p} \left(1 - \frac{A}{Z^2}\right) y_s(p), \quad (2)$$

diffusion calculations give  $R \sim 5$  (Bildsten et al. 1992). As  $j_p \propto \dot{m}$ , where  $\dot{m}$  is mass accretion rate per unit area, therefore Equation (2) can be re-expressed in terms of  $\dot{m}$  as

$$t_{\text{exposure}} \approx \frac{0.5(\text{kg cm}^{-2})}{\dot{m}(\text{kg cm}^{-2} \text{ s}^{-1})} \left(1 - \frac{A}{Z^2}\right). \quad (3)$$

$t_{\text{exposure}}$  for the elements carbon, neon, silicon, and iron over a range of mass accretion rates per unit area are shown in Figure 1. There are two observations worth noting. First, for a given element the exposure time decreases with increasing mass accretion rate per unit area. Second, for a given  $\dot{m}$  the exposure time for different elements is nearly the same. We therefore assume for the remainder of this work that for a given mass accretion rate per unit area the exposure time is independent of the element, and use the exposure time of  $^{12}\text{C}$  for all elements.

The spallation process is modeled using the NucNet Tools single-zone reaction network.<sup>9</sup> Along with the proton-induced spallation reactions,  $\beta$ -decays were also included as the fragments produced can be unstable nuclei. The single-zone reaction network includes 486 isotopes from hydrogen to iron coupled by a total of 13,076 reactions. Out of these reactions,

<sup>9</sup> <https://sourceforge.net/p/nucnet-tools/home/Home/>

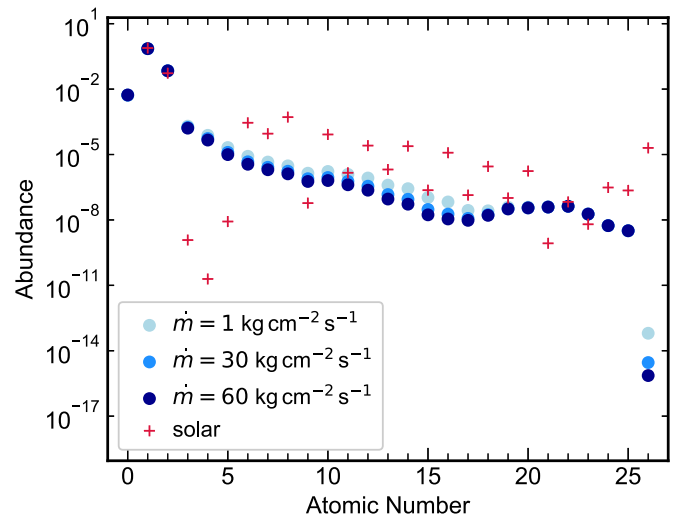


**Figure 2.** Accreted composition with and without spallation. Red crosses show the initial solar composition, whereas blue dots show the final composition after spallation for three different mass accretion rates per unit area.

1421 are weak reactions and the rest are spallation reactions. Spallation reactions were incorporated into the reaction network as decay reactions, since the protons inducing the spallation are constantly supplied by accretion.  $\beta$ -decay rates were taken from the Nuclear Wallet Cards (Tuli 2011). The spallation reaction rates were calculated as  $j_p \times \sigma(E_p)$ , where  $\sigma(E_p)$  are energy-dependent partial cross sections. The spallation cross sections  $\sigma(E_p)$  were calculated using the open-source subroutines from the work of Silberberg et al. (1998). These cross sections are based on the semi-empirical formulae of Letaw et al. (1983) and scaled to available experimental data (Gallo et al. 2019). Nevertheless, spallation cross section data for unstable nuclei are scarce and, for the many reaction channels for which data are missing, uncertainties can be as large as a factor of two or more. For a given mass accretion rate, the reaction network is evolved for the corresponding exposure time.

Hydrogen and helium have the same stopping depths (same  $A/Z^2$ ); therefore, no He spallation is considered in the present case. Helium spallation can still occur during slow down in the atmosphere, but spallation products quickly reassemble through various reactions restoring the initial amount of helium (Bildsten et al. 1993).

### 3. Spallation Results

Element abundances after spallation are shown in Figure 2 for three different exposure times corresponding to three different accretion rates. Clearly spallation can significantly reduce the accreted heavy element abundances from solar to subsolar for all elements heavier than boron. Heavier elements are affected the strongest.

In Bildsten et al. (1992), only the destruction of CNO elements was considered (isolated destruction). However, in the cascading destruction process, due to the transformation of heavier elements into CNO elements, the CNO elements are partially replenished. To check whether accounting for the full cascading process makes any difference compared to isolated destruction, we followed the abundance evolution of  $^{12}\text{C}$  in an isolated destruction process and in a full cascading process.

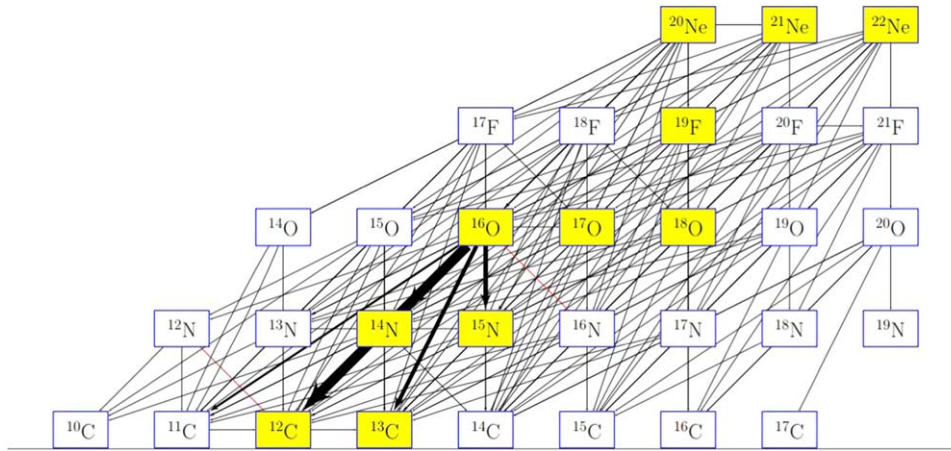


Figure 3. Time-integrated net reaction flow.

The time-integrated net reaction flow is shown in Figure 3 for isotopes from neon to carbon. The time-integrated reaction flow shows how carbon is replenished via the destruction of neon, oxygen, and nitrogen. The major path of  $^{12}\text{C}$  production is via spallation of  $^{14}\text{N}$  and  $^{16}\text{O}$ . These production channels will be missing in the isolated destruction scenario.

Figure 4 shows that the difference in carbon abundance is conspicuous for cascading and isolated destruction models for all mass accretion rates. The final carbon abundance in the isolated destruction scenario is several orders of magnitude smaller. These results demonstrate that CNO destruction can be overestimated if no replenishment is considered.

## 4. Discussion

### 4.1. Impact on the Burst Ignition Conditions

The spallation calculations in the present work show that the resulting  $Z_{\text{CNO}}$  can be as high as  $10^{-5}$  (cascading model). In order to understand the impact of  $Z_{\text{CNO}}$  on X-ray burst ignition conditions, we have used the code `settle`, which computes ignition conditions for type I X-ray bursts. `settle` uses a multi-zone model of the accreting layer and a one-zone ignition criterion (Cumming & Bildsten 2000). A simple hydrostatic model of the atmosphere during fuel accumulation and immediately prior to X-ray burst ignition is calculated. The model relies on the fact that above a certain mass accretion rate, the accumulating hydrogen is thermally stable and burns via the hot CNO cycles, i.e., the hydrogen-burning rate is constant for a given  $Z_{\text{CNO}}$  value. The change in hydrogen mass fraction  $X_{\text{H}}$  with column depth  $y$  is given by  $dX_{\text{H}}/dy = -\epsilon_{\text{H}}/mE_{\text{H}}$ , where  $\epsilon_{\text{H}}$  is the energy production rate via hot CNO cycles (which depends on  $Z_{\text{CNO}}$ ), and  $E_{\text{H}}$  is the energy release per gram from burning hydrogen to helium. Neutrino energy losses are neglected. Integrating this equation provides the hydrogen abundance as a function of depth. If helium ignites at a column depth  $y < y_{\text{d}}$  (the depth at which hydrogen runs out), a mixed hydrogen–helium–burning flash occurs; otherwise, a pure-helium layer accumulates. In order to obtain a thermal profile of the accumulating layer from the heat equation, the flux from the hot CNO cycles, and the heat released by electron captures, as well as pycnonuclear reactions in the deeper crust (base flux) are considered. Here we assume a base flux of  $0.15 \text{ MeV/u}$ . The resulting hydrogen mass fractions present at the time of ignition as a function of mass accretion rate per unit area are shown in Figure 5 for different metallicities. Figure 5 shows

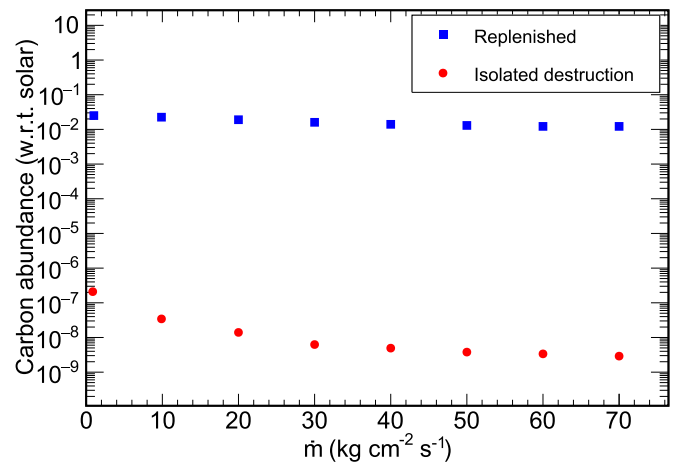


Figure 4. Abundance of carbon surviving in two different models as a function of accretion rate per unit area  $\dot{m}$ .

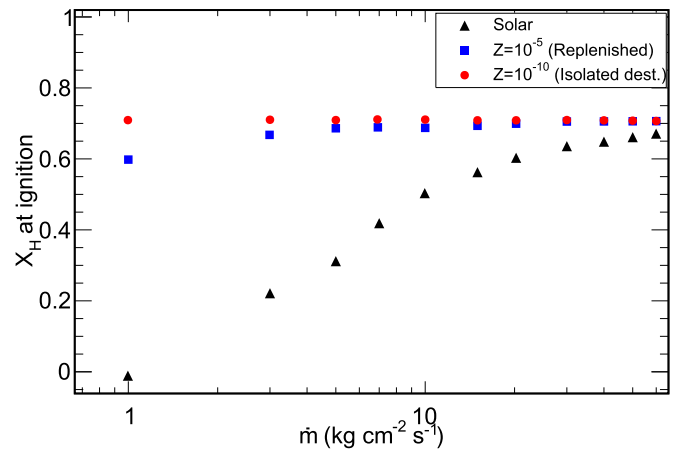


Figure 5. Hydrogen mass fraction at the base of the accumulated column during ignition for different  $Z_{\text{CNO}}$  values. We take  $M = 1.4 M_{\odot}$ ,  $R = 10 \text{ km}$  and base flux  $F_b = 0.15 \text{ MeV/u}$ . These results are obtained using the code `settle`.

that for solar  $Z_{\text{CNO}}$ , the amount of hydrogen present at the time of helium ignition decreases as the mass accretion rate decreases, and after a certain point no hydrogen is left at the time of helium ignition leading to pure-helium bursts. For  $Z_{\text{CNO}} = 10^{-10}$  (isolated destruction), a negligible amount of hydrogen is burned before the burst and hydrogen is present at

helium ignition even at low accretion rates. At these low accretion rates we find a substantial change of  $X_H$  between cascading/replenished and isolated destruction models. However, for  $\dot{m} \sim 5 \text{ kg cm}^{-2} \text{ s}^{-1}$  and below, sedimentation affects the distribution of isotopes and the ignition of H and He in the envelope of an accreting neutron star (Peng et al. 2007). Further studies are required to determine if this counteracts the effect of lower  $Z$ . Despite the differences, our results uphold the general conclusion of Bildsten et al. (1992) that spallation leads to burst ignition in a hydrogen–helium mixture for a broad range of accretion rates, even when a full cascading process is considered.

#### 4.2. Impact of Spallation-altered Accreted Composition on X-Ray Bursts Ashes

We performed 1D multi-zone hydrodynamic X-ray burst calculations with the code MESA (Paxton et al. 2010, 2013, 2015, 2018) to investigate the impact of our new spallation results on the predicted burst ashes. Calculations were performed following the methods of Meisel (2018) and Meisel et al. (2019). Briefly, these consisted of discretizing a  $0.01 \text{ km}$  atmosphere of a  $1.4 M_\odot$   $11.2 \text{ km}$  neutron star into  $\sim 1000$  zones and following the nuclear burning and hydrodynamic evolution induced by accretion. The 304 isotope network of Fisker et al. (2008) and REACLIB (Cyburt et al. 2010) v2.2 reaction rates were used. Hydrodynamic corrections included a post-Newtonian modification of the local gravity to emulate general relativistic effects, and convection was approximated using a time-dependent mixing length theory (Henyey et al. 1965; Paxton et al. 2010). MESA v9793 was used with the time resolution and spatial resolution adapting in time according to the MESA controls `varcontrol_target=1d-3` and `mesh_delta_coeff=1.0` (Paxton et al. 2013).

Accretion is achieved by adding a small amount of mass to the model’s outer layers and readjusting the stellar structure (Paxton et al. 2010). An accretion rate of  $10 \text{ kg cm}^{-2} \text{ s}^{-1}$  was used along with a base heating of  $0.15 \text{ MeV}$  per accreted nucleon.

For  $X_H = 0.70$  and  $Y = 1 - X_H - Z$ , calculations were performed with  $Z = 0.02$  (solar),  $10^{-5}$  (cascading destruction/replenishment model),  $10^{-14}$  (isolated destruction model), and 0, each assuming a scaled solar metal distribution (Grevesse & Sauval 1998). Results are shown in Figure 6. For lower  $Z$ , the resulting abundance distribution is shifted to higher mass numbers. This is expected, as reduced CNO abundances reduce hydrogen burning during accretion, leading to more hydrogen-rich conditions at burst ignition and therefore to extended hydrogen burning (Heger et al. 2007; José et al. 2010; Meisel et al. 2019). Between  $Z = 10^{-5}$  and  $10^{-14}$ , the mass fraction of isotopes summed by mass number ( $X(A)$ ) can vary by more than a factor of two (Figure 6, lower panel). The lower- $Z$  calculations show particularly large differences in the oscillating abundance pattern associated with  $A = 4n$  nuclei (Meisel et al. 2019) due to less helium-rich ignition conditions. These changes are significant relative to other changes in astrophysical conditions and nuclear reaction rates (Meisel et al. 2019). Most of the changes in  $X(A)$  are in the  $A \sim 30$ – $60$  region, which potentially affects the urca cooling neutrino luminosity in the crust (Meisel & Deibel 2017). These changes may also alter the thermal conductivity in the inner crust of the neutron star, where it is governed by electron–ion impurity scattering. Nuclear reactions in the crust funnel X-ray burst ashes in the  $A = 29$ – $55$  range into the  $N = 28$  shell closure

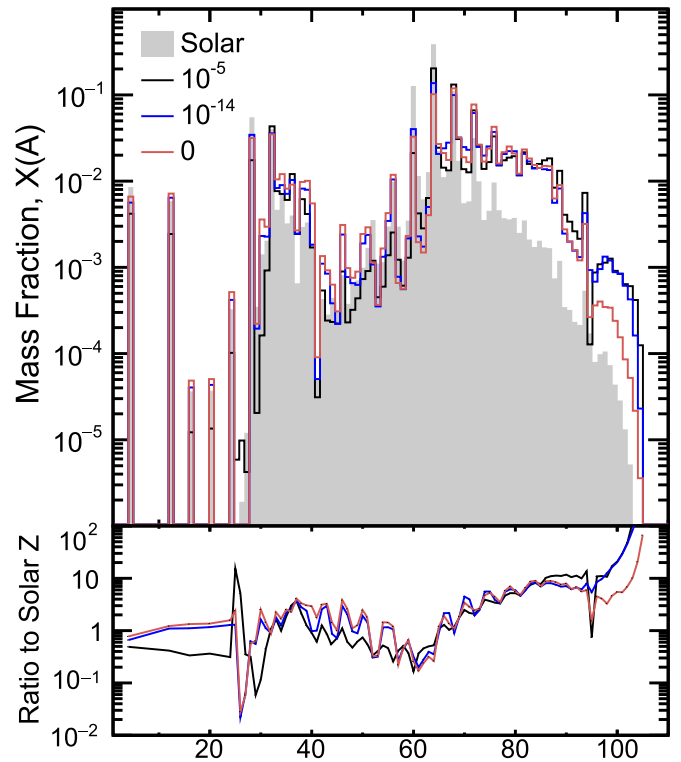


**Figure 6.** (Upper panel) Abundance as function of mass number from multi-zone X-ray burst calculations with  $X = 0.70$  and metallicity indicated by the legend. (Lower panel) Abundance ratio as function of mass number to calculations performed with solar  $Z$ .

(Lau et al. 2018) by the time the material reaches the inner crust. Changes in  $X(A)$  in this mass region (Figure 6, lower panel) therefore directly affect the inner crust impurity parameter.

A higher probability of  $^{12}\text{C}$  survival raises the question of whether this survival leads to enough carbon in the neutron star ocean to ignite the occasionally observed X-ray superbursts (Cumming & Bildsten 2001). However, the resulting carbon abundances remain many orders of magnitude below the mass fractions of the order of 20% estimated to be required to power superbursts (Cumming et al. 2006). Superburst models therefore continue to require significant carbon production by hydrogen- and helium-burning processes either in X-ray bursts or in steady state (Stevens et al. 2014). Our higher initial CNO abundances do not lead to increased carbon production in X-ray bursts (Figure 6); in fact, they rather lead to a reduction due to the lower helium abundance at burst ignition.

## 5. Conclusions

We provide new calculations of the spallation-modified composition of material accreted onto a neutron star. These are the first calculations that use a full nuclear reaction network. The resulting compositions can serve as initial parameters for X-ray burst models and differ significantly from the frequently used initial compositions based on the companion star. Our results also differ significantly from estimates of spallation models using isolated destruction processes. We find that when a full cascading destruction model and a full reaction network is used final CNO abundances are significantly larger, though still below the accreted abundances. These larger CNO

abundances, especially at lower accretion rates, alter the amount of hydrogen present at the time of burst ignition. We show that this has a significant effect on X-ray burst model predictions of the composition of the burst ashes. Our results must therefore be taken into account in X-ray burst model calculations used to predict the thermal and compositional structure of accreted neutron star crusts (Lau et al. 2018; Meisel et al. 2019).

This work is mainly the product of discussions at the 3rd Astrophysical Reaction Network School supported by the National Science Foundation under grant No. PHY-1430152 (JINA Center for the Evolution of the Elements). J.S.R and R.K. gratefully acknowledge the support from NSERC Canada for this work. Z.M. was supported in part by the U.S. Department of Energy under grant Nos. DE-FG02-88ER40387 and DESC0019042. S.A.G. acknowledges support from the U.S. Department of Energy under Award Number DOE-DE-NA0002847 (NNSA, the Stewardship Science Academy Alliances program). H.S. acknowledges support from NSF under PHY-1102511. B.S.M. was supported by NASA under grant No. NNX17AE32G.

*Software:* NucNet tools, `settle` (Cumming & Bildsten 2000), MESA (Paxton et al. 2010, 2013, 2015, 2018).

#### ORCID iDs

J. S. Randhawa  <https://orcid.org/0000-0001-6860-3754>  
 Z. Meisel  <https://orcid.org/0000-0002-8403-8879>  
 K. Ebinger  <https://orcid.org/0000-0002-0023-0864>

#### References

Bildsten, L., Salpeter, E. E., & Wasserman, I. 1992, *ApJ*, 384, 143  
 Bildsten, L., Salpeter, E. E., & Wasserman, I. 1993, *ApJ*, 408, 615

Cumming, A., & Bildsten, L. 2000, *ApJ*, 544, 453  
 Cumming, A., & Bildsten, L. 2001, *ApJL*, 559, L127  
 Cumming, A., Macbeth, J., in't Zand, J. J. M., & Page, D. 2006, *ApJ*, 646, 429  
 Cyburt, R. H., Amthor, A. M., Ferguson, R., et al. 2010, *ApJS*, 189, 240  
 Cyburt, R. H., Amthor, A. M., Heger, A., et al. 2016, *ApJ*, 830, 55  
 Fisker, J. L., Schatz, H., & Thielemann, F.-K. 2008, *ApJS*, 174, 261  
 Gallo, L. C., Randhawa, J. S., Waddell, S. G. H., et al. 2019, *MNRAS*, 484, 3036  
 Grevesse, N., & Sauval, A. 1998, *SSRv*, 85, 161  
 Heger, A., Cumming, A., Galloway, D. K., & Woosley, S. E. 2007, *ApJL*, 671, L141  
 Heney, L., Vardya, M. S., & Bodenheimer, P. 1965, *ApJ*, 142, 841  
 Jose, J. 2016, *Stellar Explosions: Hydrodynamics and Nucleosynthesis* (Boca Raton, FL, London: CRC Press, Taylor and Francis)  
 José, J., Moreno, F., Parikh, A., & Iliadis, C. 2010, *ApJS*, 189, 204  
 Lau, R., Beard, M., Gupta, S. S., et al. 2018, *ApJ*, 859, 62  
 Letaw, J. R., Silberberg, R., & Tsao, C. H. 1983, *ApJS*, 51, 271  
 Lewin, W. H. G., van Paradijs, J., & Taam, R. E. 1993, *SSRv*, 62, 223  
 Meisel, Z. 2018, *ApJ*, 860, 147  
 Meisel, Z., & Deibel, A. 2017, *ApJ*, 837, 73  
 Meisel, Z., Deibel, A., Keek, L., Shternin, P., & Elfriz, J. 2018, *JPhG*, 45, 093001  
 Meisel, Z., Merz, G., & Medvid, S. 2019, *ApJ*, 872, 84  
 Özel, F., & Freire, P. 2016, *ARA&A*, 54, 401  
 Paxton, B., Bildsten, L., Dotter, A., et al. 2010, *ApJS*, 192, 3  
 Paxton, B., Cantiello, M., Arras, P., et al. 2013, *ApJS*, 208, 4  
 Paxton, B., Marchant, P., Schwab, J., et al. 2015, *ApJS*, 220, 15  
 Paxton, B., Schwab, J., Bauer, E. B., et al. 2018, *ApJS*, 234, 34  
 Peng, F., Brown, E. F., & Truran, J. W. 2007, *ApJ*, 654, 1022  
 Schatz, H., Aprahamian, A., Barnard, V., et al. 2001, *PhRvL*, 86, 3471  
 Schatz, H., & Rehm, K. 2006, *NuPhA*, 777, 601  
 Silberberg, R., Tsao, C. H., & Barghouty, A. F. 1998, *ApJ*, 501, 911  
 Stevens, J., Brown, E. F., Cumming, A., Cyburt, R., & Schatz, H. 2014, *ApJ*, 791, 106  
 Strohmayer, T., & Bildsten, L. 2006, *Compact Stellar X-ray Sources* (Cambridge: Cambridge Univ. Press)  
 Tuli, J. K. 2011, *Nuclear Wallet Cards* (8th ed.), Brookhaven National Laboratory  
 Wallace, R. K., & Woosley, S. E. 1981, *ApJS*, 45, 389  
 Woosley, S. E., Heger, A., Cumming, A., et al. 2004, *ApJS*, 151, 75  
 Zamfir, M., Cumming, A., & Galloway, D. K. 2012, *ApJ*, 749, 69